LABORATORY-BASED BRDF CALIBRATION OF RADIOMETRIC TARPS

Georgi T. Georgiev[a], James J. Butler[b]

[a]Science Systems and Applications, Inc., Lanham, MD 20706, e-mail:
ggeorgi@pop900.gsfc.nasa.gov

[b]NASA Goddard Space Flight Center, Code 614.4, Greenbelt, MD 20771

POPULAR SUMMARY

The current study provides the remote sensing community with important high accuracy laboratory-based diffuse reflectance calibration of radiometric tarps. The measured samples are witness pieces from larger chemically treated field-deployed radiometric canvas tarps used as reference reflectance standards in remote sensing characterizations. The results illustrate the dependence of tarps' weft and warp threads orientation on the diffuse reflectance. The dependence is well defined at all measurement geometries and wavelengths. The fitted diffuse reflectance shows a very small discrepancy from the measured one. The forward and backward scatter properties of the tarps were also studied. The diffuse reflectance characterization of radiometric tarps can be successfully extended to other structured surface fabric samples. The results are NIST traceable.

LABORATORY-BASED BRDF CALIBRATION OF RADIOMETRIC TARPS

Georgi T. Georgiev[a], James J. Butler[b]

[a]Science Systems and Applications, Inc., Lanham, MD 20706, e-mail:

ggeorgi@pop900.gsfc.nasa.gov

[b]NASA Goddard Space Flight Center, Code 614.4, Greenbelt, MD 20771

ABSTRACT

The current study provides the remote sensing community with important high accuracy laboratory-based BRDF calibration of radiometric tarps. The results illustrate the dependence of tarps' weft and warp threads orientation on BRDF. The study was done at incident angles of 0°, 10°, and 30°; scatter zenith angles from 0° to 60°, and scatter azimuth angles of 0°, 45°, 90°, 135°, and 180°. The wavelengths were 485nm, 550nm, 633nm and 800nm. The dependence is well defined at all measurement geometries and wavelengths. It can be as high as 8% at 0° incident angle and 2% at 30° incident angle. The fitted BRDF data show a very small discrepancy from the measured ones. New data on the forward and backscatter properties of radiometric tarps is reported. The backward scatter is well pronounced for the white samples. The black sample has well pronounced forward scatter. The BRDF characterization of radiometric tarps can be successfully extended to other structured surface fabric samples. The results are NIST traceable.

Keywords: BRDF, Optical scattering, Metrology, Remote Sensing, Reflectance spectroscopy

1. INTRODUCTION

The ability to monitor, understands, and predicts the Earth's climate and environmental processes depends on the quality of data from Earth's remote sensing instruments. The global nature of Earth's processes requires consistent long-term calibration of all the instruments involved in data retrieval[1]. The bidirectional reflectance distribution function (BRDF) defines the directional reflection characteristics of an optical surface. It gives the reflectance of a target in a specific direction as a function of illumination and viewing geometry. The BRDF depends on wavelength and reflects the structural and optical properties of the surface. Various space and airborne radiometric and imaging remote sensing instruments use diffuse scatter plates as calibration sources requiring preflight BRDF calibration measurements[2,3]. On-board diffusers are used to trend on-orbit instrument radiance or reflectance calibration. Laboratory based diffusers are used for pre-flight instrument radiance calibrations. BRDF measurements of natural targets are also used for remote sensing characterization of vegetation canopies and soils[4], oceans[5], or especially large pollution sources[6].

The data reported in this study is intended to more completely describe the BRDF of radiometric tarp samples with particular interest on the effect of tarp weft tread orientation. This study was done in support of the commercial vicarious calibration program at NASA's Stennis Space Center, from which the samples were obtained[7,8]. They are witness pieces from larger chemically treated field-deployed radiometric canvas tarps used as reference reflectance standards in remote sensing characterizations. The radiometric tarps were also used to perform spatial characterizations measuring the sensors ability to image an edge formed by using two contrasting tarps. The tarps are manufactured with strict specifications; they are large enough to characterize the spatial characteristics of 1 m ground sample distance (GSD) class imagery. The targets can easily be deployed over alternative sites; the proper care at deployment is also of great importance. The accuracy of such tarp-based field calibrations

depend on an accurate knowledge of the tarps laboratory measured BRDF at a variety of source illumination and detector scatter angles. The reported data is traceable to NIST's Special Tri-function Automated Reference Reflectometer (STARR)[9] via test standards.

2. BACKGROUND

The radiometric tarp samples were studied in the Diffuser Calibration Facility at NASA's Goddard Space Flight Center (GSFC) using the facility's scatterometer. The scatterometer, located in a class 10000 laminar flow cleanroom, is capable of measuring the BRDF or bidirectional transmissive distribution function (BTDF) of a wide range of sample types including white diffusers, gray-scale diffusers, black painted or anodized diffusers, polished or roughened metal surfaces, clean or contaminated mirrors, transmissive diffusers, liquids, and granular solids. The operational spectral range of the instrument is from 230 nm to 900 nm. The scatterometer facilitates computerized measurements at selected incident and scattered geometries and wavelengths for complete data acquisition. The measurement uncertainty, Δ_{BRDF}, depends on several instrument variables. It was consequently evaluated in accordance with NIST guidelines[10] by Schiff[11] to be less than 1% (k=1).

The scatterometer can perform in-plane and out-of-plane BRDF and BTDF measurements, and 8° directional/hemispherical measurements. It consists of a vertical optical source table, a sample stage, a detector goniometer, and a computer system for positioning control, data collection and analysis. Fig.1 shows the instrument's optical layout. The optical table can be rotated around its horizontal axis located at the table center to change the incident angle, θ_i, relative to the sample normal. The optical source table contains two possible light sources - a 75 W xenon short-arc lamp coupled to a Chromex 250SM scanning monochromator and a He/Ne laser. Although not shown on Fig.1, additional laser sources are

possible. The xenon lamp assembly is compact and generates an output beam focused onto a monochromator entrance slit. A filter wheel is attached to the exit slit to block higher order spectra. Spherical and flat mirrors focus the output monochromatic beam onto a fixed aperture. The optical beam is then directed to the sample surface by a spherical and two flat mirrors. The incident light is linearly polarized by a Glan-Thompson polarizer. The optical path for the laser source is simpler. Flat mirrors direct the laser beam to the sample. The incident beam is collimated by two lenses and linearly polarized by a different Glan-Thompson polarizer. When measurements are made with the xenon short-arc lamp source the folding mirror for the laser beam, shown in Fig.1 with dashed line, which would block the xenon lamp beam, is removed.

Fig.2 shows the goniometer mechanism of the scatterometer. The scattered from the sample light is collected using an ultraviolet-enhanced silicon photodiode detector with output fed to a computer-controlled lock-in amplifier. The sample is mounted on a sample stage in the horizontal plane. The sample stage allows proper positioning of the sample with respect to the incident beam. It can be moved in X, Y and Z linear directions using three motors. The sample stage provides sample rotation in the horizontal plane around Z axis enabling changes in the incident azimuth angle, φ_i. The sample stage leveling is adjustable using two manual micrometers. Various holders are available to support samples of different sizes, shapes, and thicknesses. Samples can be as large as 45 cm square and up to 4.5 kg in weight. However, larger and heavier samples can be measured by using an appropriate external sample stage.

The position of the detector assembly is determined by the scatter zenith and scatter azimuth angles. The detector assembly can be rotated around the vertical, Z, and horizontal, X, Y axes of the goniometer. As shown in Fig.2 the detector moves along the arc providing the ability to make scatter measurements as a function of the scatter zenith angle, θ_s. The arc rotates 180° around the vertical Z axis which determines the scatter azimuth angle, φ_s. The center of the illuminated spot on the surface of the sample has to be positioned at the cross

point of the three perpendicular goniometer rotation axes, X, Y, Z, coinciding with the center of a sphere with radius equal to the distance between that point and the detector's assembly cover aperture.

The operation of the scatterometer is fully computerized. Custom software was developed to control all motion, data acquisition, and data analysis. The optical beams are mechanically chopped and a lock-in data acquisition technique is used. The electronics consists of a motion control module and a lock-in-amplifier. Custom pre-amp embedded into the detector housing was also designed and built.

The Diffuse Calibration Facility has participated in several round-robin[12] measurement campaigns with domestic and foreign institutions. It has supported a number of NASA and international remote sensing Earth and space projects. Among these are the Total Ozone Mapping Spectrometer (TOMS)[13], the Solar Backscatter UltraViolet 2 (SBUV/2)[14], the Shuttle-borne SBUV (SSBUV)[15], the Moderate resolution Imaging Spectroradiometer (MODIS), Landsat-7, the Ozone Mapping and Profiler Suite (OMPS), the Ozone Monitoring Instrument (OMI), and the James Webb Space Telescope (JWST). The facility has characterized many types of samples including Spectralon, Aluminum diffusers, Barium Sulfate, optical elements, Martian regolith simulant[16], and leaf litter and soil samples[17].

3. EXPERIMENT

The BRDF definition and derivation is credited to Nicodemus et al[18] who examined the problem of defining and measuring the scatter of diffuse and specular optical materials. Following his concept the scatter defining geometry is shown in Fig.3, where the subscripts *i* and *s* refer to incident and scatter quantities, respectively. Accordingly, the direction of a specular beam (forward scatter) is defined as $\theta_i = \theta_s$ at $\Delta\phi = \phi_s - \phi_i = 180°$ and backward

scatter as $\theta_i = \theta_s$ at $\Delta\phi_s = 0°$. He also assumed that all scatter comes from the sample surface and none from the bulk. He defined the BRDF in radiometric terms as the ratio of the surface radiance L_s scattered by a surface into the direction (θ_s, ϕ_s) to the incident surface irradiance E_i incident on a unit area of the surface at a particular wavelength:

$$BRDF = \frac{dL_s(\theta_i, \phi_i, \theta_s, \phi_s; E_i)}{dE_i(\theta_i, \phi_i)},\qquad(1)$$

where the subscripts i and s denote incident and scattered respectively, θ is the zenith, and ϕ is the azimuth angle.

Nicodemus further assumed that the beam has a uniform cross section, the illuminated area on the sample is isotropic, and all scatter comes from the sample surface. In practice, we are dealing with real samples' surfaces which are not isotropic and the optical beams used to measure the reflectance are not perfectly uniform. Hence from the practical considerations the BRDF can be defined, as presented by Stover[19], as the scattered power per unit solid angle normalized by the incident power and the cosine of the detector zenith angle. It is expressed in terms of incident power, scattered power and the geometry of incident and reflected light:

$$BRDF = \frac{P_s/\Omega}{P_i\cos\theta_s},\qquad(2)$$

where P_i is the incident power, P_s is the scatter power, θ_s is the detector zenith angle and Ω is the solid angle determined by the area of detector aperture, A, and the distance from the sample surface to the limiting aperture at the detector assembly, R, or $\Omega = A/R^2$.

We are using the above BRDF expression as it allows for bulk scatter in addition to surface scatter and permits non-uniform incident beam profiles. BRDF has units of inverse steradians and can range from very small numbers (e.g. off-specular black samples) to very large values (e.g. highly reflective samples at specular reflectance).

Four tarp samples all 10 cm x 10.5 cm cut along the weft and warp thread directions were studied. The samples are of similar material structure, possessing a highly regular wave-

like structure but with different reflectance. The surface structure of the samples is shown on a microscopic image of tarp sample 1 in Fig.4. The tarps were made of woven polyester duck with a protective silicone pigmented coating. The samples were mounted flat on the scatterometer sample stage. The illuminated area depends on the incident angle. It varies from 16 mm in diameter at $0°$ incident angle to an ellipse with a long axis of 28 mm at $30°$ incident angle.

The bidirectional reflectance distribution of any sample strongly depends on the direction of the incident light on the sample and the detector's position as determined by the scatter zenith and scatter azimuth angles presented in Fig.3. The incident light along the sample normal describes the sample's bidirectional reflectance distribution at normal incidence while the incident light at angles other than normal describes the bidirectional reflectance distribution at non-normal incidence. The incident and scatter angles of this study were chosen by Stennis Space Center based on the illumination geometries of their vicarious airborne calibrations. Both in-the-principal-plane and out-of-the-principal-plane scans were performed hereafter referred to as in-plane and out-of-plane. The incident angles (i.e. source zenith) were $0°$, $10°$, and $30°$; the source azimuth angle was fixed at $4°$. The in-plane scans are at scatter azimuth angles of $0°$, and $180°$. The out-of-plan scans were at scatter azimuth angles of $45°$, $90°$, and $135°$. All the scans were performed at scatter zenith angles from $0°$ to $60°$ in $5°$ steps. The wavelengths were 485, 550, 633 and 800 nm with a spectral bandwidth of 12 nm. The detector field-of-view was centered on the samples for all measurements. We used the underfilled BRDF measurement technique meaning the illuminated area on the sample was always smaller than the detector FOV. All measurements in the current study were made for polarizations of the incident beam both parallel and perpendicular to the plane of incidence. The BRDF values for both polarizations were then averaged to yield the BRDF for unpolarized incident radiant flux and the values of unpolarized scattering case are reported in this paper.

8° directional/hemispherical reflectance of the same samples was also measured. The 8° integrating sphere is a separate accessory to the scatterometer. The sphere collects and spatially integrates the scattered optical radiation. The sphere interior is Spectralon with a typical reflectance of 94% to 99% from the UV to the NIR. The sphere was designed with four ports to accommodate the sample, the detector, and the entry of the incident light. A fourth port is a spare and is typically closed using a Spectralon plug. The total port area is less than 5% of the total surface area of the sphere. It is important to have the radiation balance established inside the sphere after as few internal reflections as possible. The light intensity incident on the detector should correspond to the average light intensity inside the sphere. An interior baffle is employed to block the detector viewing light reflected directly from the sample.

4. RESULTS & DISCUSSION

The BRDF of the radiometric tarp samples is presented in Figs. 5 to 13. The tarps 8° directional/hemispherical reflectance is given in Table 7. The measured BRDF data was also fitted using a fifth-degree polynomial regression: $Y = A+Bx+Cx^2+Dx^3+Ex^4+Fx^5$ as the calibrated radiometric tarps can be used as a standard samples for remote sensing. The coefficients, A, B, C, D, E, and F, given in Tables 1 to 3, were calculated at 485 nm wavelength, a scatter azimuth angles of 0°, 45°, 90°, 135°, 180°, and an incident angles of 0°, 10° and 30° in the scatter zenith angular range from –60° to 60°. The polynomial regression can be used for deriving BRDF data at random scatter zenith angles for the above-mentioned fixed angles and wavelength. The performance was evaluated by the Root-Mean-Square Error (RMSE), the most commonly used measure of success of numeric prediction. The error has the same dimensions as the predicted values themselves. The RMSE criterion is:

$$\sigma = \sqrt{\frac{1}{N}\sum(f'-f)^2} \ , \tag{3}$$

where f' is the modeled, f is the measured BRDF and N is the number of points measured.

4.1. BRDF at normal incidence

The tarps were studied first at normal incident illumination. The BRDF of the samples was measured in-plane at $0°$ and $180°$ scatter azimuth and out-of-plane at $45°$, $90°$ and $135°$ scatter azimuth positions. The scatter zenith angles vary from $10°$ to $60°$ in $5°$ steps. The scatter zenith angle of $0°$ was not measured as at this geometry the detector is obscured by the last fold mirror. The BRDF at normal incidence of all tarp samples at wavelength of 485 nm is shown in Fig.5 for scatter azimuth angles $0°$ and $180°$. The scatter zenith angles at $0°$ scatter azimuth are presented in this figure as negative to be in accordance with the standard angular convention. In the following discussions, we will refer only to sample 1, as there are not substantial differences between the samples except their absolute reflectance.

The BRDF of sample 1 at 485 nm and at scatter azimuth angles $0°$, $45°$, $90°$, $135°$ and $180°$ is shown in Fig.6 as a function for scatter zenith angle at normal incidence illumination. The measurements at 550, 633 and 800 nm are not represented as they show the same tendencies and would be redundant. Two types of data are presented in Fig.6 – the fitted BRDF as plotted from the polynomial coefficients in Table 1, and the measured data points. The error between the modeled and measured values is calculated using the RMSE criteria described in eq.3. The values for scatter azimuth angles of $0°$, $45°$, $90°$, $135°$, and $180°$, both normal and non-normal incidence are given in Table 4 for sample 1 at 485 nm. The largest error is at normal incidence, 2.32×10^{-4}.

The surface of tarp samples is structured; therefore even at normal incidence their BRDF depends on the weft and warp thread orientation. The scatter from the surface depends mainly on the scatter zenith angle. However the weft bumps obscure the detector from

viewing the full surface. Therefore the scatter also depends on the scatter azimuth angle whether the detector scan plane is perpendicular or not to the weft threads. The BRDF should be higher where the tarp weft threads lie parallel to the detector scan plane as then the obscuration is minimal. The maximum obscuration occurs where the detector scan plane is perpendicular to the weft threads, corresponding to lower BRDF. The scatter zenith angle contributes to the obscuration effect as the obscuration if higher at larger scatter zenith angles. The BRDF of tarp 1 is given in Fig.6. The highest BRDF was recorded at $0°$ and $180°$ scatter azimuth where the tarp weft threads lie parallel to the detector scan plane. The BRDF decreases at $45°$ and $135°$ scatter azimuth angles as the detector rotates to an orientation $45°$ relative to the sample weft threads. The lowest BRDF was measured at $90°$ scatter azimuth, in accordance with our expectations.

The data in Table 5 show what difference the observer should expect at airborne measurements depending on the scatter zenith angle, if assumed the source (Sun) is at zenith. The data in this table represent the deviation in the tarp optical scattering from Lambertian. To make the comparison simpler we designate the BRDF at $30°$ scatter zenith as a reference and compare the BRDF at other scatter zenith angles to the $30°$ value. The BRDF differences were calculated from the BRDF data of sample 1 at 485 nm, normal incidence, and scatter azimuth angles of $0°$, $45°$, $90°$, $135°$, and $180°$. It was found that the difference could be as high as 13% for a $5°$ scatter zenith angle. The BRDF difference on the scatter zenith angle decreases as the wavelength increases. For example the difference between BRDF at $30°$ and $5°$ scatter zenith is 13.02% at 485 nm and 8.83% at 800 nm. The difference between BRDF at $30°$ and $60°$ scatter zenith is –6.65% at 485 nm increasing to 2.76% at 800 nm.

The dependence of BRDF on wavelength at normal incidence for sample 1 is given in Fig.7 at 485, 550, 633 and 800 nm at scatter azimuth of $0°$ and $180°$. The BRDF doesn't change at small scatter zenith angles, while at larger scatter zenith angles the BRDF increases with the wavelength. The detector scan plane is parallel to the weft threads at scatter azimuth

angles of $0°$ and $180°$ and perpendicular to them at a scatter azimuth angle of $90°$. The BRDF dependence on the weft threads is best addressed when the BRDF at scatter azimuth angles of $0°$ and $90°$ are compared. In this use the weft threads influence is presented in Fig.8 for sample 1, for wavelengths of 485, 550, and 633 nm. For clarity of presentation the BRDF at 800 nm is omitted from the figure as it does not give any new information. The difference in BRDF of sample 1 at a scatter azimuth $0°$ vs. the BRDF at a scatter azimuth of $90°$ is also presented in Table 7 at 485, 550, 633, 800 nm. Table 6 summarizes data for both normal and non-normal incidence. However in this section we present the normal incidence related data only. The data obtained at non-normal incidence will be commented in the respective section. The BRDF measured at a scatter azimuth of $90°$ is used as a reference. Since the BRDF at $0°$ is always higher than at $90°$, the data in the Table are negative. The difference at normal incidence could be as high as -7.99% at $60°$ scatter zenith at 485 nm and as low as -1.17% at $10°$ scatter zenith at 633 nm. The difference in BRDF at $0°$ vs. $90°$ increases with scatter zenith angle for all wavelengths at normal incidence. It is also higher at shorter wavelengths. Although not presented, the results of samples 2, 3 and 4 show the same characteristics. The variation in BRDF is due to the weft obscuring effect of the weft structure translated into the data at normal incidence.

4.2. BRDF at non-normal incident angles

The BRDF of the tarp samples at non-normal incident angles is different from that at normal incidence. The difference is mainly due to the non-isotropic structure of sample's surface. The partial obscuration of the detector view by the weft bumps was already commented for the case of normal incidence. The same effect is observed at non-normal incidence plus the additional shadowing effect of the same weft bumps on the incident to the surface light. The weft rows (i) partially obscure the detector view and (ii) the shadow they cast reduces the illuminated area of the sample. The two effects reduce the observed BRDF.

The relative and absolute straights of these effects depends on the incident angle, scatter zenith and azimuth angles, and the orientation of the weft threads relative to the plane of the incident light.

In the process of characterizing the sample BRDF data we fitted the measured points using a standard polynomial procedure, similar to what we used at normal incidence. The coefficients of the polynomial regression are given in Tables 2 and 3 according to the wavelength and measurement geometry for 10° and 30° incident angles. The polynomial regression can be used for deriving BRDF data at random scatter zenith angles at fixed scatter azimuth angles at 485 nm. The fitting procedure was applied for scatter zenith angles from 0° to 60° except at 180° scatter azimuth where it was applied from 15° to 60° due to the detector obscuration at 10° scatter zenith. Two polynomials were used to model the BRDF at the 30° incident angle geometry, one for 0° to 25° scatter zenith and one for 35° to 60° scatter zenith as the detector is obscured at the 30° scatter zenith angle.

BRDF versus scatter zenith angle. BRDF data was acquired at 10° and 30° incident angles for 0°, 45°, 90°, 135° and 180° scatter azimuth positions on all samples. The scatter zenith angles vary from 0° to 60° in 5° steps. The BRDF of sample 1 at 485 nm is presented in Figs.9 and 10 for 10° and 30° incident angles, respectively. The BRDF of samples 2, 3 and 4 as well as the measurements at 550, 633 and 800 nm are not presented as they show the same scattering tendencies. Two types of data are presented in the figures – the fitted BRDF curve and the measured points. The fitted curves are plotted from the polynomial coefficients as given in Table 2 for 10° and Table 3 for 30° incident angles.

The BRDF at 10° incidence angle was seen to decrease to different extent with increasing scatter zenith angle for 0°, 45°, and 90° scatter azimuth independently of wavelength for all samples. The BRDF data at 180° scatter azimuth follow the tendency as discussed for the case of normal incidence. The BRDF in the principal plane is higher at scatter zenith angles closest to the angle of incidence. The BRDF at 135° scatter azimuth

follow the same pattern although the BRDF values are lower than those measured at 180° scatter azimuth.

Fig.10 shows the BRDF at 30° incident angle and 485 nm for 0°, 45°, 90°, 135° and 180° scatter azimuth. The BRDF follows the same pattern as at the 10° incident angle. However the BRDF at 180° scatter azimuth is significantly higher than the BRDF at other scatter azimuth angles and at smaller scatter zenith angles.

Backward and Forward scatter. The BRDF at non-normal incidence describes the forward and backward scattering properties of the tarps. The backscatter is calculated by simply taking the difference of the BRDF at scatter zenith angles symmetric to the sample normal. Tarps 1, 2, 3, called "white" tarps hereafter exhibit well-pronounced backward scattering, better expressed at larger incident angles for both 10° and 30° incident angles as shown for tarp 1 in Fig.11. The "white" tarps' backward scattering is better pronounced at shorter wavelengths. However the scattering of tarp 4, the "black" tarp, is quite different. This sample has well pronounced forward scattering properties as shown in Fig.12, especially at 30° incident angle. The forward scattering is also very well visible for higher than 25° scatter zenith angles at 10° incidence angle.

It is not unusual for black materials to have different scatter distributions than lighter samples. The tarps used in remote sensing calibrations are generally treated with a pigment of titanium dioxide and carbon black and coated with a silicone pigment. The carbon black exhibits strong forward scattering properties[20]. In general, the black materials exhibit a higher degree of polarization through reflection compared to the white materials. We believe the forward scattering properties demonstrated by the black sample are due to the carbon black used at the manufacturing process and its polarization properties.

BRDF spectral dependence. The BRDF spectral dependence based on data measured at wavelengths of 485, 550, 633 and 800 nm is shown in Fig.13. BRDF of tarp 1 at incident angle 30°, scatter azimuth angles of 0° and 180° is presented for scatter zenith angles from 0°

to 60°, in 10° steps. The BRDF spectral dependence at non-normal incidence follows the same pattern as at normal incidence, that is, the BRDF increases with the wavelength. All the samples were found to have the same spectral dependence, including the black sample. However the BRDF data of the black sample in the visible (485, 550, 633nm) were very similar, only the BRDF at 800 nm being higher. This makes the black sample BRDF properties spectrally indifferent in the visible range.

4.3. 8° directional/hemispherical measurement

The 8° directional/hemispherical reflectance of all the tarp samples was measured with a HeNe laser at 632.8 nm. The only hardware difference from the experimental setup described in the previous section is the use of an 8° directional/hemispherical integrating sphere mounted above the scatterometer sample stage. The silicon photodiode detector was fixed to one port of the sphere. The relationship between sample reflectance and detector signal can be parameterized using Spectralon samples of known reflectance. We chose a 3rd order polynomial for this parameterization. The coefficients of the polynomial were calculated by fitting the receiver power measured with a set of 7 gray Spectralon standard targets of nominal reflectance 5%, 10%, 20%, 40%, 60%, 80% and 99% with known 8° directional/hemispherical reflectance. The measured 8° directional/hemispherical reflectance data for each sample are given in Table 7.

5. CONCLUSIONS

The BRDF results of four radiometric tarp samples calibrated at NASA's GSFC Diffuse Calibration Facility show a strong dependence on the weave orientation relative to the measurement geometry. The experimental data shows that the weft and warp threads

orientation has a clear effect on BRDF for both normal and non-normal incident angles. Non-normal incident angles introduce an additional dependence of BRDF on weave orientation. BRDF differences vary and can approach 13.5% for non-normal incidence and 8% for normal incident angle. There is also a spectral dependence on BRDF, which is apparent at higher scatter zenith angles over the spectral range from 485 to 800 nm for both normal and non-normal incidence. The fitted BRDF values show a very small discrepancy from the measured ones in both normal and non-normal incident angles. The highest RMSE was calculated to be 2.32×10^{-4} sr^{-1}. The provided polynomial coefficients can be used for calculating the BRDF at random scatter zenith angles. The forward and backward scatter properties of the tarps were also studied. The backward scatter is well pronounced for the "white" samples – tarps 1, 2 and 3. Tarp 4, the "black" sample, has well pronounced forward scatter. Our current understanding is that the forward scatter is induced by the used at manufacturing carbon black due to its polarization properties. The 8° directional/hemispherical reflectance data complements the BRDF measurements.

The current study provides the remote sensing community with important high accuracy BRDF calibration data of radiometric tarps used in the vicarious calibrations of satellite instruments. The BRDF data obtained from these studies is important for future NASA SSC vicarious calibrations through analysis of the BRDF dependence on weft, warp threads orientation. The BRDF characterization of tarp samples as shown in this paper can be successfully extended to other structured surface fabric samples.

ACKNOWLEDGEMENTS

REFERENCES

1.   J.J. Butler, B.C. Johnson, R.A. Barnes, "The calibration and characterization of Earth remote sensing and environmental monitoring instruments", in Optical Radiometry, Ed. A.C. Parr, R.U. Datla, J.L. Gardner, Academic Press, New York (2005).

2.   G.B. Courreges-Lacoste, J.G. Schaarsberg, R. Sprik, S. Delward, "Modeling of Spectralon diffusers for radiometric calibration in remote sensing", *Opt. Eng.*, **42**, 3600-3607 (2003).

3.   C.J. Bruegge, A.E. Stiegman, R.A. Rainen and A.W. Springsteen, "Use of Spectralon as a diffuse reflectance standard for in-flight calibration of earth-orbiting sensors", *Opt. Eng.*, **32**, 805-814 (1993).

4.   C.K. Gatebe, M.D. King, S. Platnick, G.T. Arnold, E.F. Vermote, B. Schmid, "Airborne spectral measurements of surface-atmosphere anisotropy for several surfaces and ecosystems over southern Africa", *J. Geophysical Research*, **108**, D13, 25-1-16 (2003).

5.   C.K. Gatebe, M.D. King, A.I. Lyapustin, G.T. Arnold, J. Redemann, "Airborne spectral measurements of ocean directional reflectance", *J. Atmospheric Sciences*, **62**, 1072-1092 (2005).

6.   M.D. King, "Directional and spectral reflectance of the Kuwait oil-fire smoke", *J. Geophysical Research*, **97**, D13, 14545-14549 (1992).

7.   S. Blonski, M. Pagnutti, R.E. Ryan, V. Zanoni, "In-flight edge response measurements for high-spatial-resolution remote sensing systems", *Proc. SPIE*, **4814**, 317-326 (2002).

8.   M. Pagnutti, R. Ryan, M. Kelly, K. Holekamp, V. Zanoni, K Thome, S. Schiller, "Radiometric characterization of IKONOS multispectral imagery" *Remote Sensing of Environment*, **88**, 53-68 (2003).

9.	J.R. Proctor and P.Y. Barnes, "NIST High accuracy reference reflectometer - spectrophotometer", *J. Res. Nat. Inst. Stand. Technol.*, **101**, 619-627 (1996).

10.	B.N. Taylor and C. E. Kuyatt, "A Guidelines for Evaluating and Expressing the Uncertainty of NIST Measurement Results", NIST Technical Note 1297, U.S. Department of Commerce, National Institute of Standards and Technology, Sep. 1997.

11.	T.F. Schiff, M.W. Knighton, D.J. Wilson, F.M. Cady, J.C. Stover, and J.J. Butler, "A Design Review of a High Accuracy UV to Near Infrared Scatterometer", *Proc. SPIE, 1995*, 121-130 (1993).

12.	E.A. Early, P.Y. Barnes, B.C. Johnson, J.J. Butler, C.J. Bruegge, S.F. Biggar, P.S. Spyak and M.M. Pavlov, "Bidirectional Reflectance Round-Robin in Support of the Earth Observing System Program", *J. Atmospheric and Oceanic Techn*, **17**, 1077-1091 (2000).

13.	J.J. Butler, H. Park, P.Y. Barnes, E.A. Early, C. van Eijk-Olijd, A.E. Zoutman, S. van Buller-Leeuwend, J.G. Schaarsbergd, "Comparison of ultraviolet Bi-directional Reflectance Distribution Function (BRDF) measurements of diffusers used in the calibration of the Total Ozone Mapping Spectrometer (TOMS)", *Proc. SPIE*, **4881**, 345-354 (2003).

14.	G.T. Georgiev, J.J. Butler: "Long-term comparison of spectralon BRDF measurements in the ultraviolet", *Proc. SPIE Earth Observing Systems IX*, **5542**, 323-333 (2004).

15.	S. Janz, E. Hilsenrath, J.J. Butler, D.F. Heath, R.P. Cebula, "Uncertainties in radiance calibrations of backscatter ultraviolet (BUV) instruments", *Metrologia*, **32**, 637-641 (1995).

16.	G.T. Georgiev, J.J. Butler, "Bidirectional reflectance distribution function and directional/hemispherical reflectance of Martian regolith simulant", *Optical Engineering*, **44**, 036202 (2005).

17.	G.T. Georgiev, C.K. Gatebe, J.J. Butler, M.D. King, "Comparison between laboratory and airborne BRDF measurements for remote sensing", *Proc. SPIE Earth Observing Systems XI*, **6296**, 629603, 2006.

18.   F.E. Nicodemus, J.C. Richmond, J.J. Hsia, I.W. Ginsburg, and T. Limperis, "Geometrical considerations and nomenclature for reflectance", National Bureau of Standards, NBS monograph 160, Oct. 1977.

19.   J.C. Stover, "Optical scattering: measurement and analysis", SPIE Press, Bellingham, Washington, 1995.

20.   S. Smith, J.C. Fleming, "BRDF measurements of a new IR black coating with lower reflectance", *Proc. SPIE*, **3426**, 333-343 (1998).

Table 1: Polynomial coefficients of the samples at normal incidence, 485 nm

Coefficients	Scatter azimuth				

Sample 1

	0	45	90	135	180
A	0.20825	0.20184	0.20172	0.20113	0.20614
B	-3.69548×10^{-3}	-2.52895×10^{-3}	-2.95644×10^{-3}	-2.80741×10^{-3}	-3.32718×10^{-3}
C	1.63404×10^{-4}	6.91565×10^{-5}	9.51081×10^{-5}	9.11978×10^{-5}	1.36292×10^{-4}
D	-4.18955×10^{-6}	-9.95396×10^{-7}	-2.02885×10^{-6}	-1.99668×10^{-6}	-3.43818×10^{-6}
E	5.37358×10^{-8}	3.71795×10^{-9}	2.31818×10^{-8}	2.33217×10^{-8}	4.48814×10^{-8}
F	-2.68175×10^{-10}	2.5641×10^{-11}	-1.07692×10^{-10}	-1.07692×10^{-10}	-2.31976×10^{-10}

Sample 2

A	0.16405	0.16329	0.15781	0.16607	0.16417
B	-3.52082×10^{-3}	-3.80467×10^{-3}	-2.95437×10^{-3}	-4.54988×10^{-3}	-3.73089×10^{-3}
C	1.41832×10^{-4}	1.67633×10^{-4}	9.67351×10^{-5}	2.19402×10^{-4}	1.62164×10^{-4}
D	-3.40202×10^{-6}	-4.48153×10^{-6}	-2.16148×10^{-6}	-6.30198×10^{-6}	-4.10819×10^{-6}
E	4.10483×10^{-8}	6.01981×10^{-8}	2.6352×10^{-8}	9.06993×10^{-8}	5.18333×10^{-8}
F	-1.91855×10^{-10}	-3.12821×10^{-10}	-1.28205×10^{-10}	-5.02564×10^{-10}	-2.5098×10^{-10}

Sample 3

A	0.10311	0.0977	0.0995	0.0974	0.10218
B	-2.38324×10^{-3}	-1.55687×10^{-3}	-2.07108×10^{-3}	-1.61648×10^{-3}	-2.29836×10^{-3}
C	9.63805×10^{-5}	4.05597×10^{-5}	6.94231×10^{-5}	4.15026×10^{-5}	9.2933×10^{-5}
D	-2.25495×10^{-6}	-6.38753×10^{-7}	-1.5035×10^{-6}	-6.49476×10^{-7}	-2.1905×10^{-6}
E	2.69601×10^{-8}	5.20979×10^{-9}	1.7669×10^{-8}	5.34965×10^{-9}	2.65967×10^{-8}
F	-1.26998×10^{-10}	-1.53846×10^{-11}	-8.20513×10^{-11}	-1.53846×10^{-11}	-1.28205×10^{-10}

Sample 4

A	0.01092	0.01005	8.46818×10^{-3}	9.39545×10^{-3}	0.01039
B	-2.41551×10^{-4}	-1.29779×10^{-5}	2.42244×10^{-4}	5.50635×10^{-5}	-1.08233×10^{-4}
C	1.3284×10^{-5}	-7.4528×10^{-6}	-2.24962×10^{-5}	-9.82197×10^{-6}	1.75257×10^{-6}
D	-3.65361×10^{-7}	3.98485×10^{-7}	7.69172×10^{-7}	3.85839×10^{-7}	5.11758×10^{-8}
E	4.59345×10^{-9}	-7.71562×10^{-9}	-1.16667×10^{-8}	-6.18881×10^{-9}	-2.0074×10^{-9}
F	-2.14178×10^{-11}	5.12821×10^{-11}	6.66667×10^{-11}	3.58974×10^{-11}	1.71946×10^{-11}

Table 2: Polynomial coefficients of the samples at 10 deg incidence, 485 nm

Coefficients	Scatter azimuth				

Sample 1

	0	45	90	135	180
A	0.18296	0.18354	0.18312	0.18365	0.28976
B	-1.20021×10^{-3}	-9.69627×10^{-4}	1.11966×10^{-4}	1.74708×10^{-3}	-0.01248
C	2.15828×10^{-5}	2.51107×10^{-6}	-9.95822×10^{-5}	-2.2565×10^{-4}	5.94409×10^{-4}
D	-1.37951×10^{-7}	3.74383×10^{-7}	3.87859×10^{-6}	7.98647×10^{-6}	-1.5002×10^{-5}
E	-1.79899×10^{-9}	-8.2586×10^{-9}	-6.19032×10^{-8}	-1.23052×10^{-7}	1.88765×10^{-7}
F	2.32278×10^{-11}	5.3997×10^{-11}	3.59276×10^{-10}	7.01357×10^{-10}	-9.31282×10^{-10}

Sample 2

A	0.13859	0.13867	0.13873	0.13875	0.24535
B	-1.36321×10^{-3}	-9.63364×10^{-4}	-2.23778×10^{-4}	1.74996×10^{-3}	-0.01204
C	3.90652×10^{-5}	-2.29028×10^{-6}	-6.973×10^{-5}	-2.19264×10^{-4}	5.41148×10^{-4}
D	-9.58556×10^{-7}	5.30793×10^{-7}	2.82008×10^{-6}	7.65497×10^{-6}	-1.26653×10^{-5}
E	1.33374×10^{-8}	-1.02153×10^{-8}	-4.4891×10^{-8}	-1.16757×10^{-7}	1.46154×10^{-7}
F	-7.30015×10^{-11}	6.36501×10^{-11}	2.6003×10^{-10}	6.61538×10^{-10}	-6.5641×10^{-10}

Sample 3

A	0.08608	0.08612	0.08621	0.08609	0.14903
B	-9.23378×10^{-4}	-6.93915×10^{-4}	-1.81439×10^{-4}	1.09972×10^{-3}	-6.82608×10^{-3}
C	2.54172×10^{-5}	1.76028×10^{-6}	-4.5006×10^{-5}	-1.40507×10^{-4}	2.94509×10^{-4}
D	-4.75932×10^{-7}	3.40265×10^{-7}	1.89407×10^{-6}	4.89841×10^{-6}	-6.80331×10^{-6}
E	5.38599×10^{-9}	-7.49074×10^{-9}	-3.05882×10^{-8}	-7.39696×10^{-8}	7.92075×10^{-8}
F	-2.62443×10^{-11}	5.12821×10^{-11}	1.79487×10^{-10}	4.14178×10^{-10}	-3.65128×10^{-10}

Sample 4

A	9.48484×10^{-3}	9.48213×10^{-3}	9.51946×10^{-3}	9.50271×10^{-3}	0.01512
B	-1.9931×10^{-5}	-1.30863×10^{-5}	-2.16218×10^{-5}	6.22498×10^{-5}	-7.10272×10^{-4}
C	-2.58155×10^{-6}	-3.54336×10^{-6}	-2.97816×10^{-6}	-1.06857×10^{-5}	3.47308×10^{-5}
D	1.91907×10^{-7}	2.05142×10^{-7}	1.17267×10^{-7}	4.06767×10^{-7}	-8.93986×10^{-7}
E	-4.0436×10^{-9}	-3.96682×10^{-9}	-1.6221×10^{-9}	-6.59948×10^{-9}	1.14219×10^{-8}
F	2.7451×10^{-11}	2.6546×10^{-11}	8.74811×10^{-12}	3.92157×10^{-11}	-5.74359×10^{-11}

Table 3: Polynomial coefficients of the samples at 30 deg incidence, 485 nm

Coeff.	Scatter azimuth, deg					
	0°	45°	90°	135°	180°	
				Scatter zenith	0° to 25°	35° to 60°

Sample 1

A	0.16484	0.16479	0.16483	0.16467	0.1648	2.6852
B	-7.09245×10^{-4}	-4.62207×10^{-4}	2.03307×10^{-4}	7.44778×10^{-4}	6.15333×10^{-4}	-0.24781
C	1.45158×10^{-5}	1.4295×10^{-5}	-2.61323×10^{-5}	-7.18017×10^{-6}	5.76667×10^{-5}	9.959×10^{-3}
D	-1.93459×10^{-7}	-6.41475×10^{-7}	5.84595×10^{-7}	-7.11261×10^{-7}	-3.83333×10^{-6}	-2.01367×10^{-4}
E	7.59633×10^{-10}	1.23776×10^{-8}	-6.8696×10^{-9}	1.65611×10^{-8}	9.33333×10^{-8}	2.04×10^{-6}
F	8.44646×10^{-12}	-7.93364×10^{-11}	3.68024×10^{-11}	-1.06486×10^{-10}	8×10^{-10}	-8.26667×10^{-9}

Sample 2

A	0.1226	0.12245	0.12244	0.12249	0.1225	2.5561
B	-7.37016×10^{-4}	-3.02171×10^{-4}	1.98946×10^{-4}	6.47981×10^{-4}	3.90333×10^{-4}	-0.23511
C	1.38939×10^{-5}	-1.48631×10^{-5}	-3.30949×10^{-5}	-4.34286×10^{-6}	1.34167×10^{-4}	9.2725×10^{-3}
D	-1.89946×10^{-7}	6.02033×10^{-7}	8.51464×10^{-7}	-7.23382×10^{-7}	-1.30333×10^{-5}	-1.837×10^{-4}
E	7.65117×10^{-10}	-8.85918×10^{-9}	-1.02797×10^{-8}	1.55492×10^{-8}	5.53333×10^{-7}	1.82×10^{-6}
F	8.74811×10^{-12}	4.97738×10^{-11}	5.33937×10^{-11}	-9.2006×10^{-11}	-7.2×10^{-9}	-7.2×10^{-9}

Sample 3

A	0.07348	0.0735	0.07351	0.0735	0.0735	1.4191
B	-4.83623×10^{-4}	-2.90567×10^{-4}	6.10769×10^{-5}	3.87863×10^{-4}	6.41333×10^{-4}	-0.12745
C	8.17157×10^{-6}	-2.45451×10^{-6}	-1.10758×10^{-5}	3.42037×10^{-6}	-4.03333×10^{-5}	4.96017×10^{-3}
D	-1.1751×10^{-8}	2.9118×10^{-7}	3.14452×10^{-7}	-3.62923×10^{-7}	6.2×10^{-6}	-9.72×10^{-5}
E	-1.3177×10^{-9}	-5.86727×10^{-9}	-3.9627×10^{-9}	4.70725×10^{-9}	-3.06667×10^{-7}	9.53333×10^{-7}
F	1.68929×10^{-11}	4.19306×10^{-11}	2.05128×10^{-11}	-1.56863×10^{-11}	5.86667×10^{-9}	-3.73333×10^{-9}

Sample 4

A	8.88778×10^{-3}	8.90136×10^{-3}	8.90407×10^{-3}	8.88484×10^{-3}	8.9×10^{-3}	0.1738
B	-8.611×10^{-7}	-2.09143×10^{-5}	4.48396×10^{-6}	-1.71592×10^{-5}	-1.05×10^{-4}	-0.01642
C	1.76189×10^{-8}	5.2077×10^{-7}	-2.16554×10^{-6}	2.1775×10^{-6}	2.75×10^{-5}	6.58667×10^{-4}
D	-2.36323×10^{-8}	-2.6704×10^{-7}	9.82723×10^{-8}	-1.52969×10^{-7}	-2.56667×10^{-6}	-1.32667×10^{-5}
E	1.28891×10^{-10}	5.53819×10^{-9}	-1.91828×10^{-9}	3.03579×10^{-9}	1×10^{-7}	1.33333×10^{-7}
F	3.01659×10^{-12}	-3.65008×10^{-11}	1.44796×10^{-11}	-1.93062×10^{-11}	-1.33333×10^{-9}	-5.33333×10^{-10}

Table 4: The Root-Mean-Square Error, sr^{-1}, sample 1, 485 nm

Incident angle, deg	Scatter azimuth, deg					
	0°	45°	90°	135°	180°	
0°	2.32x10^{-4}	1.37x10^{-4}	1.20^{-4}	6.87x10^{-5}	8.88x10^{-5}	
10°	1.53x10^{-04}	2.06x10^{-04}	1.73x10^{-04}	2.86x10^{-04}	1.60x10^{-04}	
30°	1.81x10^{-04}	1.71x10^{-04}	1.85x10^{-04}	1.98x10^{-04}	1.22x10^{-13}	6.78x10^{-09}

Table 5: The BRDF difference from a reference (BRDF at 30° scatter zenith) measured at corresponding scatter zenith and azimuth angles, at normal incidence, sample 1, 485 nm

Scatter zenith, deg	Scatter azimuth, deg				
	0°	45°	90°	135°	180°
5	13.02%				13.35%
10	8.28%	9.70%	11.17%	10.59%	9.10%
15	5.66%	6.58%	7.58%	7.25%	5.98%
20	3.22%	3.85%	4.77%	4.50%	3.53%
25	1.52%	2.08%	2.44%	2.12%	1.82%
30	0.00%	0.00%	0.00%	0.00%	0.00%
35	-1.51%	-1.54%	-1.91%	-1.90%	-1.52%
40	-2.75%	-3.13%	-3.63%	-3.53%	-2.77%
45	-3.70%	-4.77%	-5.34%	-5.29%	-4.05%
50	-4.99%	-6.19%	-7.10%	-6.68%	-5.04%
55	-5.98%	-7.57%	-8.56%	-7.75%	-6.04%
60	-6.65%	-8.28%	-10.06%	-8.84%	-7.06%

Table 6: BRDF difference at scatter azimuth 0° vs 90°, %, sample 1, 90° is the base

Scatter zenith	485 nm	550 nm	633 nm	800 nm
Normal incidence				
10°	-2.00%	-1.74%	-1.17%	-1.29%
15°	-2.89%	-2.32%	-2.16%	-2.02%
20°	-3.34%	-2.82%	-2.95%	-2.35%
25°	-4.03%	-3.86%	-3.37%	-2.74%
30°	-4.85%	-4.06%	-4.04%	-3.39%
35°	-5.26%	-4.57%	-4.70%	-3.72%
40°	-5.74%	-5.28%	-4.88%	-4.20%
45°	-6.33%	-5.90%	-5.42%	-4.87%
50°	-6.94%	-6.31%	-5.70%	-4.71%
55°	-7.37%	-6.70%	-6.59%	-5.05%
60°	-7.99%	-7.10%	-6.64%	-5.40%
10° incident angle				
0°	0.00%	0.00%	0.14%	0.00%
5°	-2.06%	-1.69%	-1.41%	-1.77%
15°	-5.57%	-4.97%	-4.51%	-4.02%
20°	-4.68%	-4.01%	-3.72%	-3.22%
25°	-4.91%	-4.13%	-3.79%	-3.09%
30°	-5.18%	-4.19%	-4.15%	-3.49%
35°	-5.59%	-4.90%	-4.20%	-3.80%
40°	-5.91%	-5.12%	-4.72%	-4.14%
45°	-6.64%	-6.24%	-5.42%	-4.79%
50°	-6.89%	-6.10%	-5.63%	-4.82%
55°	-7.82%	-7.01%	-6.58%	-5.65%
60°	-8.24%	-6.89%	-6.59%	-5.66%

30° incident angle

0°	0.00%	0.00%	-0.18%	-0.15%
5°	-0.03%	0.12%	0.18%	0.15%
10°	-0.94%	-0.48%	-0.42%	-0.70%
15°	-2.63%	-1.98%	-2.12%	-1.76%
20°	-5.75%	-4.76%	-4.12%	-3.98%
25°	-10.51%	-8.82%	-7.98%	-7.01%
35°	-13.46%	-11.60%	-11.06%	-9.71%
40°	-11.76%	-9.82%	-9.11%	-8.26%
45°	-11.56%	-9.57%	-9.01%	-8.46%
50°	-11.34%	-9.82%	-9.22%	-8.63%
55°	-11.42%	-10.12%	-9.44%	-9.15%
60°	-12.04%	-11.03%	-10.30%	-9.80%

Table 7: 8° directional/hemispherical reflectance at 632.8 nm

Sample	Hemispherical Reflectance
1	67.34%
2	49.65%
3	31.93%
4	4.35%

FIGURE CAPTIONS

Fig.1: Scatterometer optical setup

Fig.2: Scatterometer goniometer mechanism

Fig.3: Geometry of incident and reflected elementary beams

Fig.4: Microscopic image of tarp sample 1, where the weft (tight) threads are horizontal and warp (woven) threads are vertical

Fig.5: In-plane BRDF of tarps 1 to 4 at normal incidence, 485nm, $0°$ and $180°$ scatter azimuth

Fig.6: BRDF of tarp 1 at normal incidence, at different scatter azimuth angles, 485nm, model and experimental points

Fig.7: BRDF of tarp 1 at normal incidence, 485, 550, 633, and 800 nm, $0°$ and $180°$ scatter azimuth angle

Fig.8: BRDF of tarp 1 at normal incidence, 485, 550, and 633 nm, $90°$ scatter azimuth angle

Fig.9: BRDF of tarp 1 at $10°$ incidence at different scatter azimuth angles, 485nm, model and experimental points

Fig.10: BRDF of tarp 1 at $30°$ incidence at different scatter azimuth angles, 485nm, model and experimental points

Fig.11: Forward – Backward scatter, tarp 1, 485 and 800 nm, $10°$ and $30°$ incident angle

Fig.12: Forward – Backward scatter, tarp 4, 485 and 800 nm, $10°$ and $30°$ incident angle

Fig.13: Tarp sample 1 at $30°$ incidence, 485nm, 550nm, 633nm, and 800nm
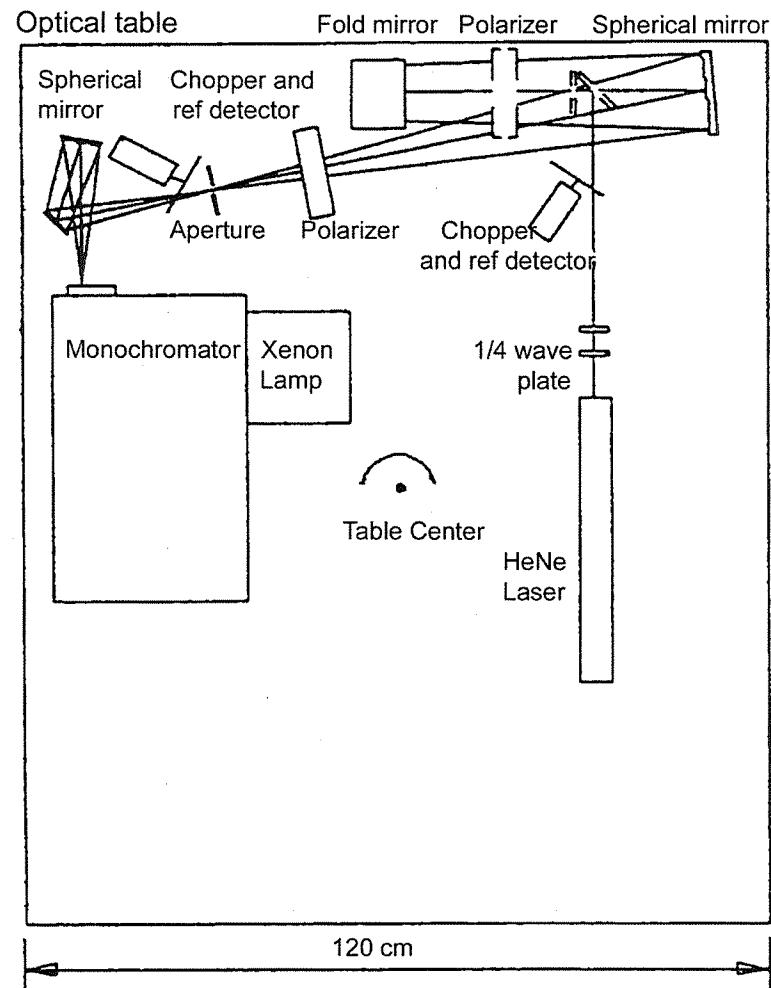
Fig.1: Scatterometer optical setup
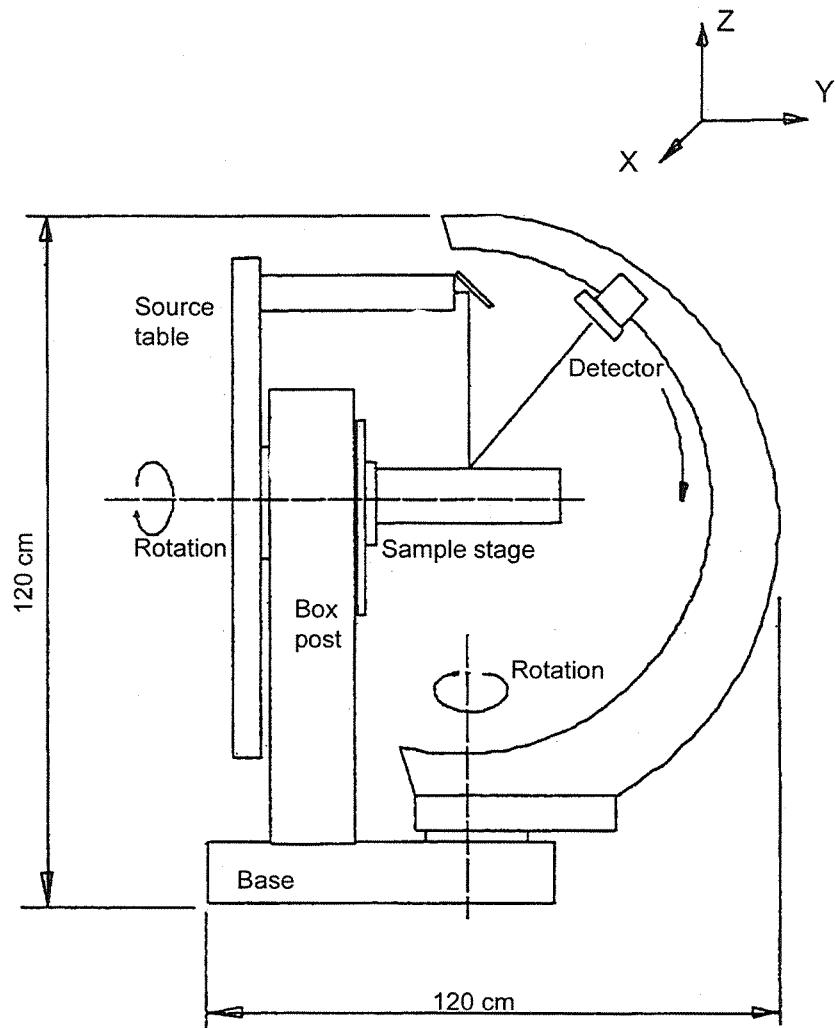
Fig.2: Scatterometer goniometer mechanism
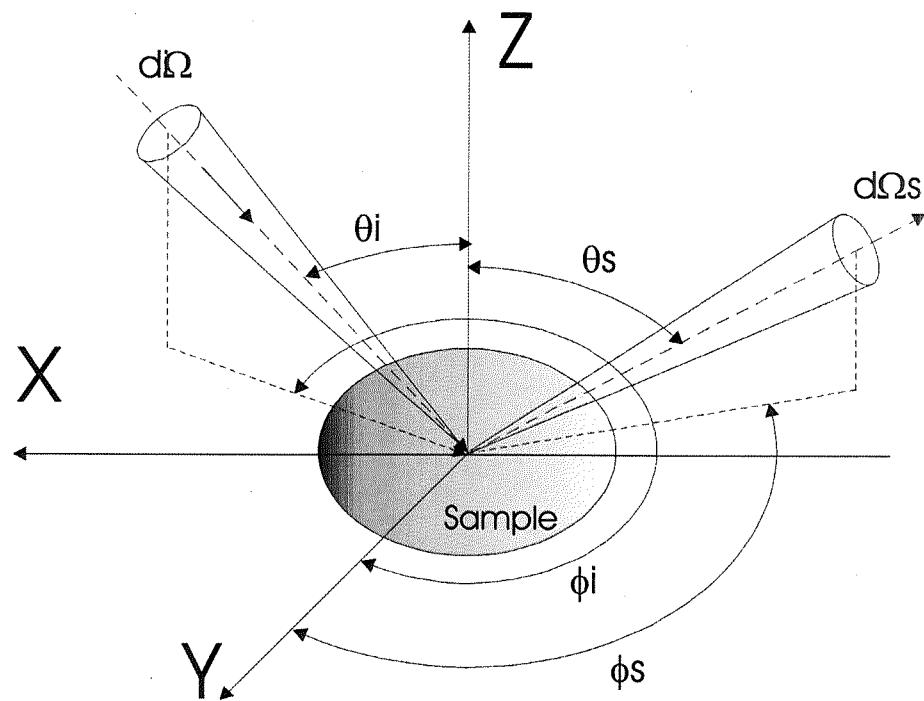
Fig.3: BRDF function incident and scattered radiation geometry after Nicodemus
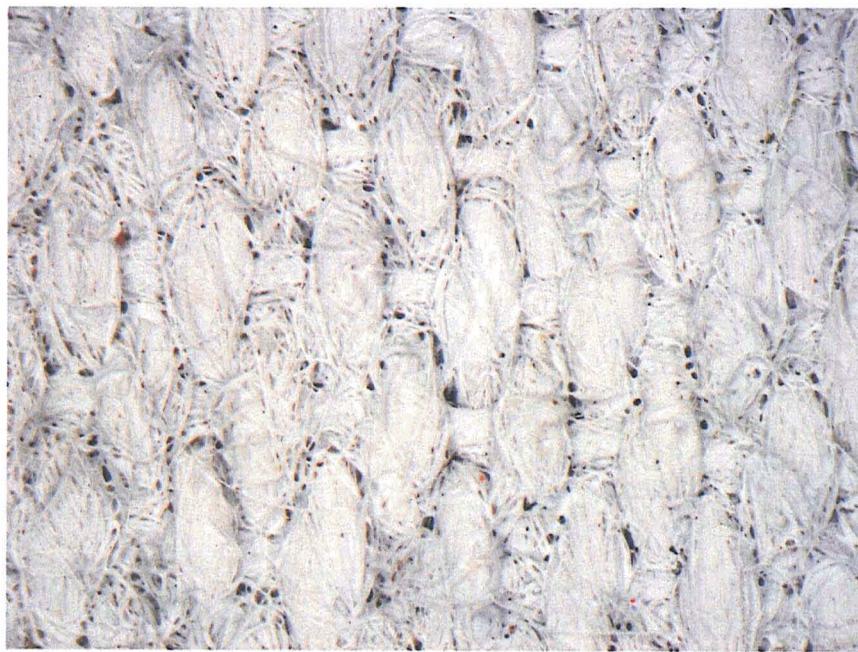
Fig.4: Microscopic image of tarp sample 1, where the weft (tight) threads are horizontal and warp (woven) threads are vertical
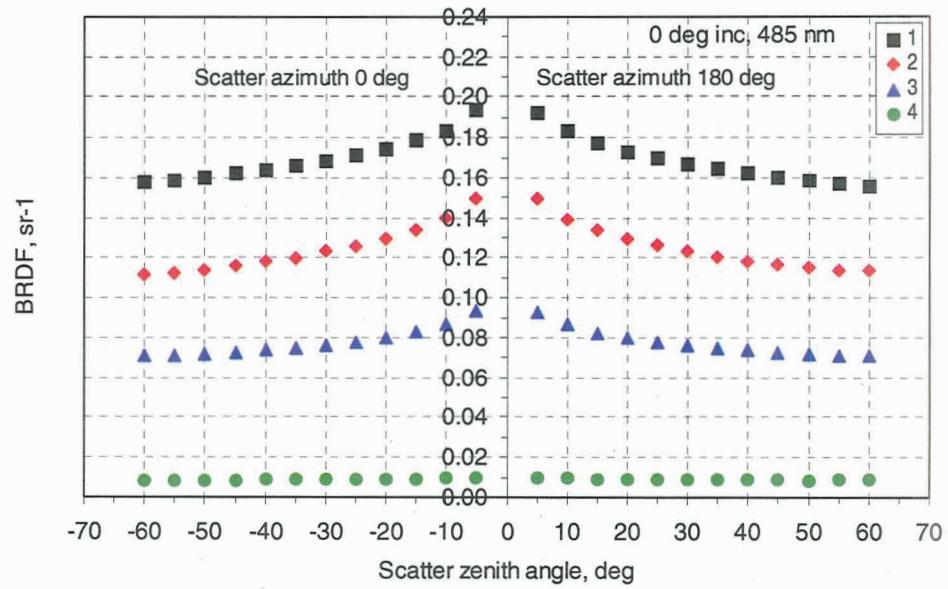
Fig.5: In-plane BRDF of tarps 1 to 4 at normal incidence, 485nm, 0° and 180° scatter azimuth
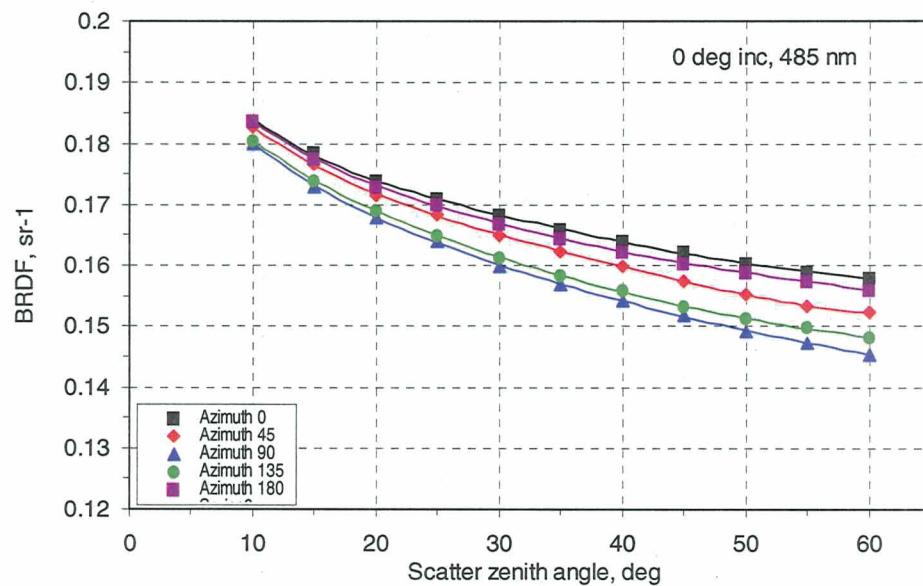
Fig.6: BRDF of tarp 1 at normal incidence at different scatter azimuth angles, 485nm, model

and experimental points
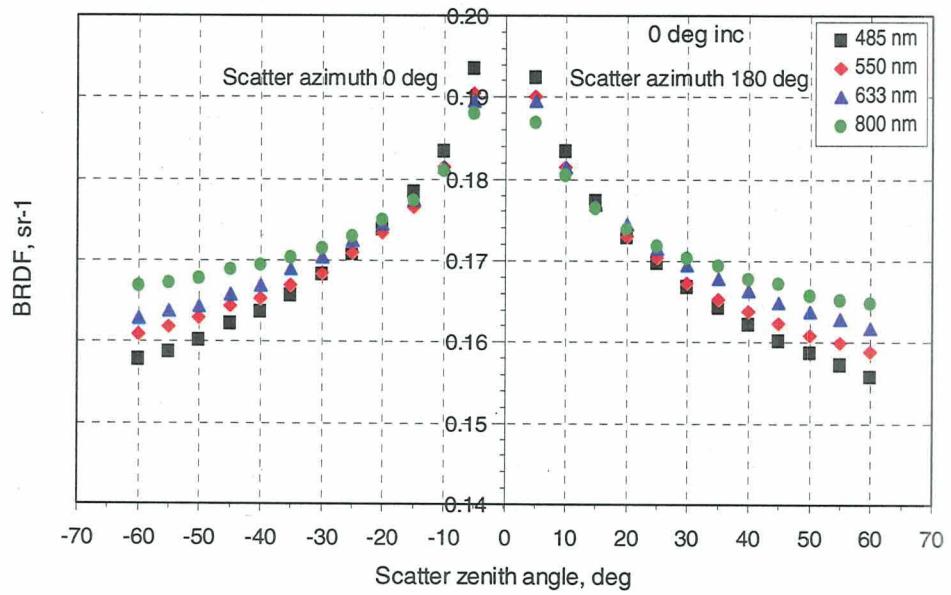
Fig.7: BRDF of tarp 1 at normal incidence, 485, 550, 633, and 800 nm, 0° and 180° scatter
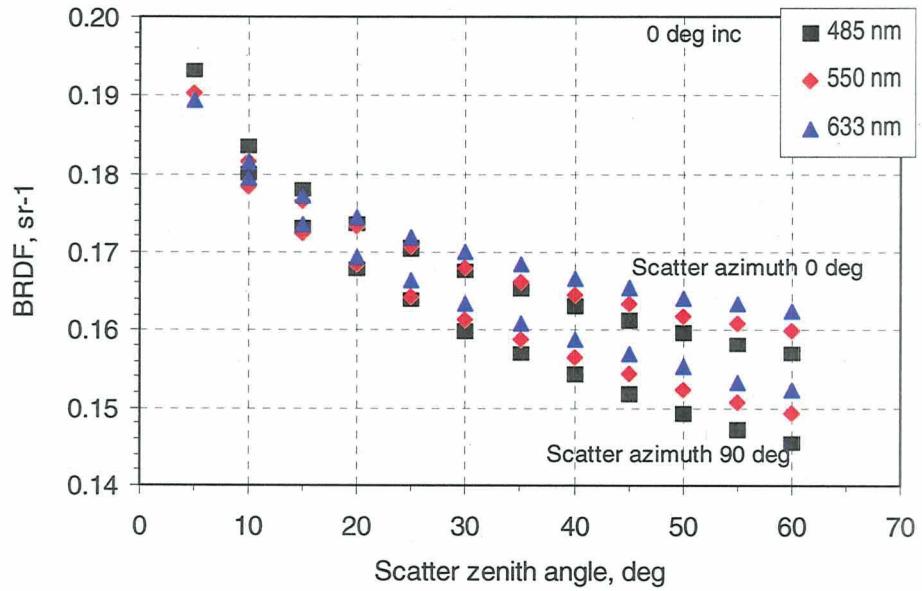
azimuth angles

Fig.8: BRDF of tarp 1 at normal incidence, 485, 550, and 633 nm, 0° and 90° scatter azimuth
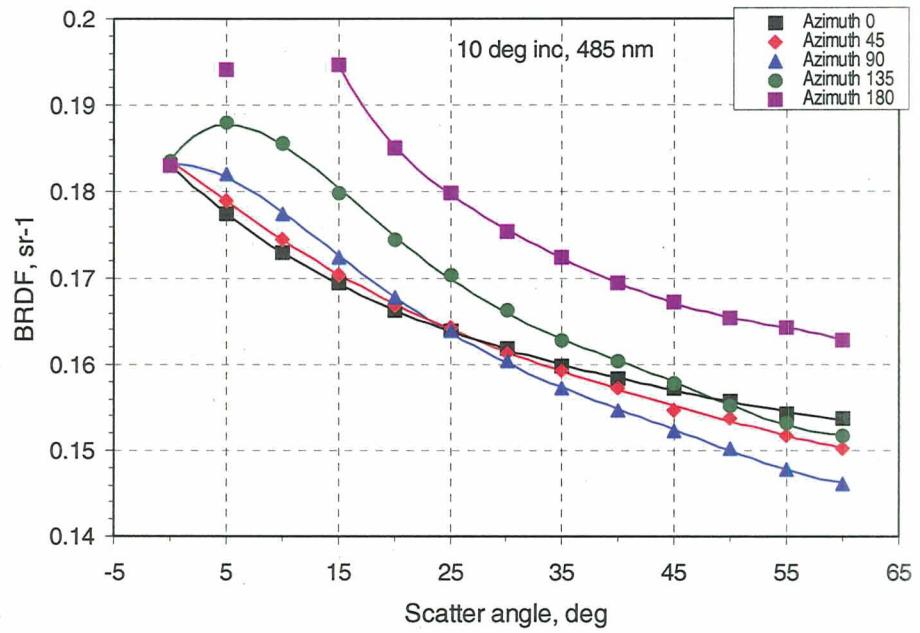
angles

Fig.9: BRDF of tarp 1 at 10° incidence at different scatter azimuth angles, 485nm, model and experimental points
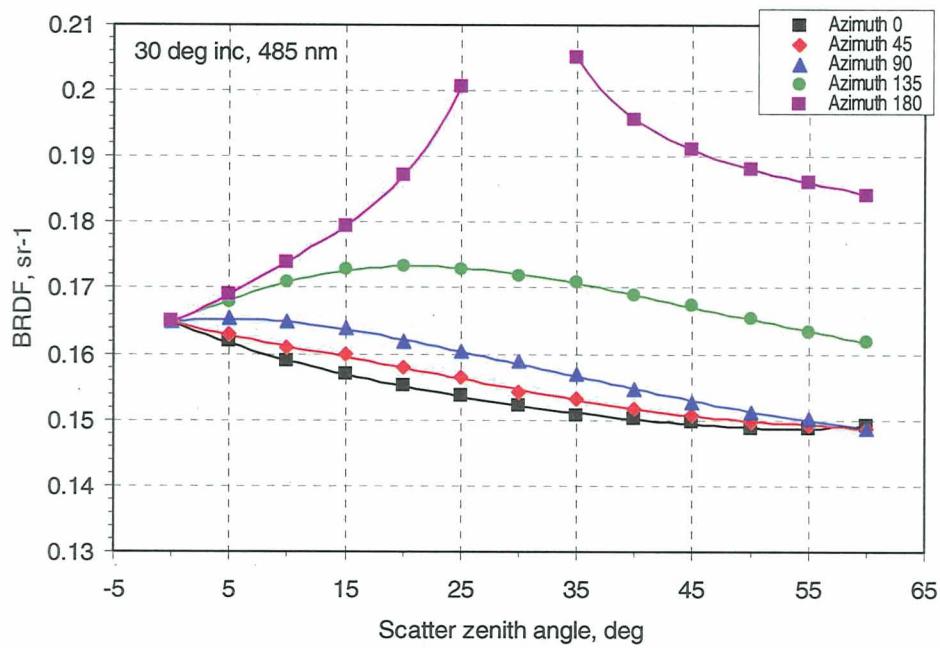
Fig.10: BRDF of tarp 1 at 30° incidence at different scatter azimuth angles, 485nm, model and experimental points
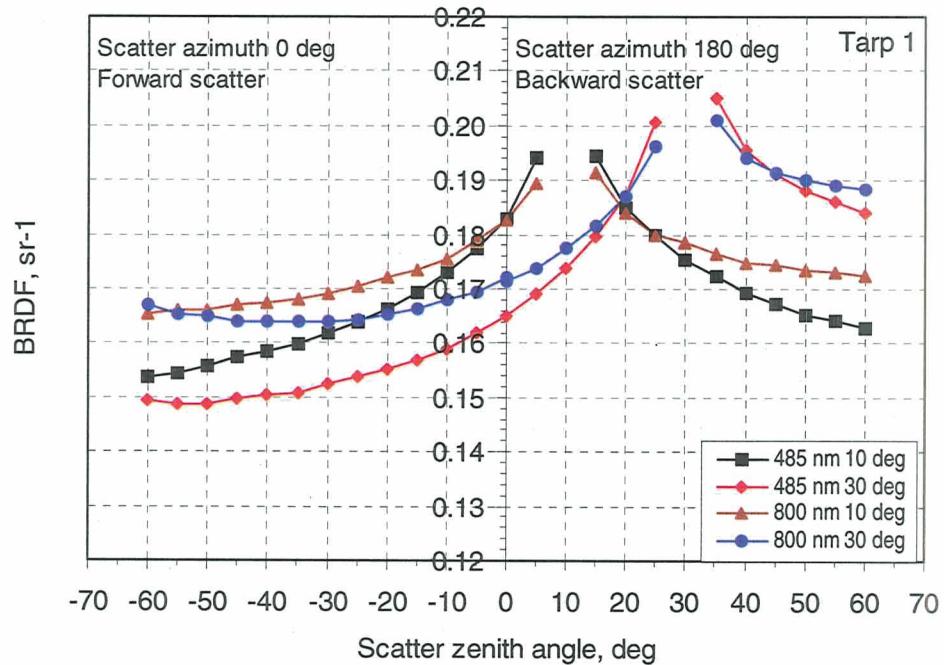
Fig.11: Forward – Backward scatter, tarp 1, 485 and 800 nm, 10° and 30° incident angles

Fig.12: Forward – Backward scatter, tarp 4, 485 and 800 nm, 10° and 30° incident angle

Fig.13: Tarp sample 1 at 30° incidence, 485nm, 550nm, 633nm, and 800nm